JGR Space Physics

RESEARCH ARTICLE
10.1029/2019JA027086

Evolution of Pitch Angle-Distributed Megaelectron Volt Electrons During Each Phase of the Geomagnetic Storm

Megha Pandya[1], Veenadhari Bhaskara[1], Yusuke Ebihara[2], Shrikanth G. Kanekal[3], and Daniel N. Baker[4]

[1]Indian Institute of Geomagnetism, Navi Mumbai, India, [2]Research Institute for Sustainable Humanosphere, Kyoto University, Uji, Japan, [3]NASA Goddard Space Flight Center, Greenbelt, MD, USA, [4]Laboratory for Atmospheric and Space Physics, Boulder, CO, USA

Key Points:
- Storm time electron pitch angle distributions (PADs) at $L = 5$ peak on the dayside, while it turns butterfly like on the nightside
- At $L = 3$, PADs of electrons do not change significantly between prestorm and at-storm intervals
- Magnetic field during at storm interval (B_{at}) decreases on the nightside, while increasing on the dayside

Correspondence to:
B. Veenadhari,
bveena@iigs.iigm.res.in

Citation:
Pandya, M. M., Bhaskara, V., Ebihara, Y., Kanekal, S. G., & Baker, D. N. (2020). Evolution of pitch angle distributed MeV electrons during each phase of the geomagnetic storm. *Journal of Geophysical Research: Space Physics*, *125*, e2019JA027086. https://doi.org/10.1029/2019JA027086

Received 2 JUL 2019
Accepted 13 DEC 2019
Accepted article online 26 DEC 2019

Abstract Using Relativistic Electron Proton Telescope measurements onboard Van Allen Probes, the evolution of electron pitch angle distributions (PADs) during the different phases of magnetic storms is studied. Electron fluxes are sorted in terms of storm phase, L value, energy, and magnetic local time (MLT) sectors for 55 magnetic storms from October 2012 through May 2017. To understand the potential mechanisms for the evolution of electron PADs, we fit PADs to a sinusoidal function $J_0 sin^n(\alpha_{eq})$, where α_{eq} is the equatorial pitch angle and n is a real number. The major inferences from our study are (i) at L~5, the prestorm electron PADs are nearly isotropic (n~0), which evolves differently in different MLT sectors during the main phase subsequently recovering back to nearly isotropic distribution type during the storm recovery phase; (ii) for $E \leq 3.4$ MeV, the main phase electron PADs become more pancake like on the dayside with high n values (>3), while it becomes more flattop to butterfly like on the nightside, (iii) at $L = 5$, magnetic field strength during the storm main phase enhances during the daytime and decreases during the nighttime. (iv) Conversely, at L ~3, the electron PADs neither respond significantly to the different phase of the magnetic storm nor reflect any MLT dependence. (v) Main phase, electron fluxes with E <4.2 MeV shows a persistent 90° maximum PAD with n ranging between 0 and 2, while for $E \geq 4.2$ MeV the distribution appears flattop and butterfly like. Our study shows that the relativistic electron PADs depend upon the geomagnetic storm phase and possible underlying mechanisms are discussed in this paper.

1. Introduction

The dynamics of the Earth's radiation belts is significantly influenced by the relativistic electron (>1 MeV) populations. The trapped radiation environment, consisting of megaelectron volt electrons, is divided into two regions, namely, the inner radiation belt and the outer radiation belt with the region separating the belts is called the slot region (2 <L <3). However, recent results from Van Allen Probes have shown that the outer zone can split into multiple belts or "storage rings" (Baker et al., 2013). The inner belt is relatively stable but exhibits a finite variations during geomagnetically active periods (e.g., Baker et al., 1986). The outer radiation belt electrons are very dynamic (Blake et al., 1992; Friedel et al., 2002) due to the complexity of the mechanisms of electron acceleration, transport, and loss (Kanekal, 2006; Li et al., 2007; Reeves et al., 2003; Turner et al., 2014). Reeves et al. (2003) showed that the megaelectron volt electron fluxes in the outer radiation belt can be enhanced, depleted, or not affected at all following a geomagnetic storm.

Recently, since the launch of the National Aeronautics and Space Administration's Van Allen Probes, the dynamics of relativistic electrons has gained renewed attention. Radiation belt electrons are influenced by the changes in magnetic field configuration, the dynamical energization and loss processes, which are reflected in electron pitch angle distributions (PADs) on different spatial and temporal scales. Electron PADs depend on factors like electron energy, spatial location, and magnetic activity. PADs of relativistic electrons provide important information to understand not only the radial distribution but also the loss and acceleration mechanisms occurring at a specific L value and different energies, for example, as shown by Baker et al. (1986). The most commonly observed electron equatorial PADs in the radiation belts include pancake PADs, butterfly PADs and flattop PADs. Pancake PADs are highly anisotropic electron velocity distribution, peaked at 90° to the magnetic field and were first detected by Wrenn et al. (1979). This distribution is also

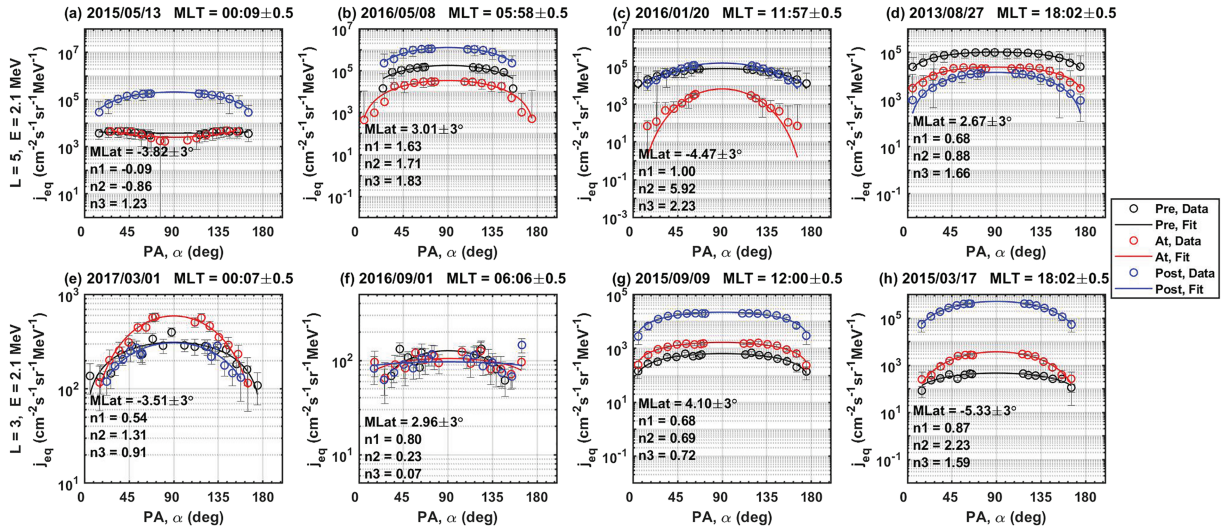

Figure 1. Examples of energetic (2.1 MeV) electron PADs, measured by REPT instrument at $L = 5$ (a–d) and $L = 3$ (e–h) in four different MLT sectors. Black, red, and blue corresponds to the electron flux measurements during prestorm, at-storm, and poststorm intervals, while circle and solid lines indicate the observed data and fitted function, respectively.

referred to as "trapped" distributions (Carbary et al., 2011) that is expected to result from wave-particle interactions or the inward radial diffusion (e.g., Schulz & Lanzerotti, 1974). Butterfly PADs have a minimum flux around 90° pitch angle (PA) and peaks at around 45° and 125° indicating magnetopause shadowing, drift shell splitting, or wave-particle interactions (e.g., West et al., 1973). When the isotropic fluxes are observed at large PAs, the distribution is called the flattop PAD, which is expected to result from strong wave-particle interactions (Horne et al. (2003). The PA diffusion coefficients are function of both energy and PA. Theoretical modeling by Thorne et al. (2005) shows that the combined effect of energy diffusion and dependence of local rate of PA scattering $D_{\alpha\alpha}$ for whistler waves leads to the development of flat-topped PADs (Horne et al. (2003). However, we note that there exist few more types of electron PADs like cigar cap as explained in Figure 1 of Zhao et al. (2018).

To understand the possible mechanisms responsible for the electron PAD evolution, we fit the PADs to a form of $J_0 sin^n(\alpha_{eq})$, where α_{eq} is the equatorial PA, J_0 is the flux at 90° PA (i.e., the constant of equation) and power "n" describes the steepness of the flux peak around 90°. Many researchers have performed the similar fitting by using CRRES and POLAR missions (e.g., Gannon et al., 2007; Selesnick & Kanekal, 2009; Vampola, 1997). However, there are several difficulties while fitting some of the electron PADs, such as butterfly PADs. For such cases, a single parameter fit is insufficient, and a set of orthogonal functions is needed. Hence, researchers like Chen et al. (2014) conducted a statistical survey on outer belt electrons and developed a new empirical model—REPAD, using Legendre polynomials to fit long-term electron fluxes observed by CRRES, Polar, and LANL-97A. Butterfly distributions generally are due to drift shell splitting, which is more significant at higher L shells than the ones explored in this paper. For example, even at $L = 5$ (Figure 1a) a "weak" butterfly type PAD is seen in the midnight sector only. The $sin^n(\alpha_{eq})$ function with a negative value of n yielded a reasonable fit to the observations. Therefore, we use the simpler approach of fitting the PADs to a single variable function. Applying the full set of trigonometric functions entails more fitting coefficients, and they are difficult to handle and interpret. Hence, we continue to adapt the representation of the form $J_0 sin^n(\alpha_{eq})$ that is simplified to a single variable.

Lyons and Williams (1975a) and Lyons and Williams (1975b) studied the quiet and active time structure of energetic 35- to 560-keV electrons at $L = 2$–4 and found that the quiet time PADs can be explained by resonance interactions with plasmaspheric hiss, while the active time PADs are greatly distorted but recover back to prestorm equilibrium structure over a period of a few weeks and then remain unchanged. West et al. (1973) studied ~80 keV to 2.8 MeV electron PAD at different local times and found that for <9 R_E the PADs are energy dependent, while at higher distances butterfly PAD dominates in the midnight sector. The combined effects of drift shell splitting and magnetopause shadowing or radial gradient are considered as the potential source of butterfly PADs in midnight (e.g., Selesnick & Blake, 2002; Sibeck et al., 1987). Recent

Table 1
List of CME- and CIR-Driven Magnetic Storms

Sr no.	CME-driven storms	Sym-H	CIR-driven storms	Sym-H
1	2012-10-01/03:52	−138	2013-01-26/22:19	−62
2	2012-10-09/02:10	−116	2013-03-01/10:12	−76
3	2012-11-14/07:27	−118	2013-03-29/16:17	−64
4	2013-03-17/20:28	−132	2013-08-27/21:43	−64
5	2013-06-01/07:48	−137	2013-10-30/23:20	−57
6	2013-06-29/06:36	−111	2013-12-08/08:30	−72
7	2013-07-06/08:33	−80	2014-06-08/06:50	−72
8	2013-10-02/06:19	−90	2015-02-17/23:55	−70
9	2014-02-19/08:23	−127	2015-02-24/03:36	−76
10	2014-02-27/23:24	−101	2015-03-02/08:51	−70
11	2014-04-12/08:32	−92	2015-04-16/23:29	−88
12	2014-04-30/09:10	−76	2015-05-13/06:59	−98
13	2014-08-27/18:18	−90	2015-06-08/07:45	−105
14	2014-09-12/23:03	−97	2015-07-05/04:52	−58
15	2015-01-07/11:00	−135	2015-07-13/10:54	−71
16	2015-03-17/22:47	−234	2015-10-07/22:23	−124
17	2015-06-23/04:24	−208	2016-01-20/16:42	−95
18	2015-07-23/07:28	−83	2016-02-03/02:52	−60
19	2015-08-16/07:37	−94	2016-02-18/00:28	−60
20	2015-08-27/20:32	−101	2016-03-06/21:20	−110
21	2015-09-09/08:03	−113	2016-05-08/08:15	−105
22	2015-11-07/06:05	−106	2016-07-25/17:17	−51
23	2015-12-20/22:49	−170	2016-08-03/06:49	−63
24	2015-12-31/23:56	−99	2016-08-23/21:13	−83
25	2016-03-06/21:20	−110	2016-09-02/01:53	−74
26	2016-04-14/08:00	−68	2016-09-29/09:32	−64
27	2016-10-13/23:45	−114	2017-03-01/22:17	−74
28			2017-03-27/14:45	−86

study by Zhao et al. (2014) report electron PADs with minimum at 90° PA, that is, butterfly PADs at low L values (i.e., inner belt and slot region) although for energies much lower than considered here. However, existing theories cannot explain these complex dynamics of inner belt and slot region. Ni et al. (2016) statistically analyzed the characteristics of outer zone relativistic electrons giving rise to butterfly distributions. They have shown that nearly 80% of the butterfly PADs are observed to occur in 20–04 magnetic local time (MLT) at $L > 5.5$, while nearly 50% them are observed at 11–15 MLT at $L{\sim}4$. Recently, Zhao et al. (2018) constructed an empirical radiation belt model that provides a statistical picture of electron PAD in the inner belt and slot region. They have shown that during a geomagnetic storm, the inner belt and slot region electrons show a minimum at 90° and that these PADs persist.

In the present study, we specially emphasize to focus on the response of PA-distributed electrons in not only different MLT sectors, L value, and over a wide range of energies but also during each phase of a magnetic storm. Unlike previous studies, we do not restrict our analysis to any particular type of electron PADs and investigate the detailed global occurrence pattern of relativistic electrons. Using high-quality and comprehensive data collected by the Relativistic Electron Proton Telescope (REPT) instrument onboard Van Allen Probes, we hope to advance our understanding of the radiation belt dynamics. Our paper is organized as follows. Section 2 deals with the description of the satellite data and methodology. Section 3 gives the observation and results of electron flux variations at different L range and PA. Section 4 discusses our results and summary.

2. Data and Methodology

We investigate the PADs of relativistic electron flux with the geomagnetic activity from October 2012 to May 2017. We select the geomagnetic storms having minimum Sym-H being less than −50 nT and classified them based on their solar drivers, namely, Coronal Mass Ejection (CME) and Corotating Interaction Region (CIR). We have used the 1-min-resolved symmetric component of ring current (Sym-H) high-resolution data set from online OMNIWEB data service. The present analysis is an extension of the work by Pandya et al. (2019) that examined the role of CIRs and CMEs in the electron dynamics at different L values. For our present analysis, the list of CME- and CIR-driven magnetic storms is taken from Pandya et al. (2019) (shown in Table 1). For each magnetic storm, the electron fluxes are separated during the inbound and outbound passages of Van Allen Probes A orbit and averaged over each storm phase. We also retain the MLT information. Hence, we have 110 observations (inbound + outbound) corresponding to 55 geomagnetic storms, during each phase of the magnetic storm.

For this study, PA-resolved electron flux data from the REPT (Baker et al., 2012) instruments of Energetic Particle, Composition, and Thermal Plasma suite (Spence et al., 2013) on Van Allen Probes from October 2012 to May 2017 are used. It is a twin spacecraft having orbital period of ~9 hr, with an elliptical orbit of ~600 km × 5.8 R_E and an inclination of approximately 10°, launched in August 2012. The REPT instrument can sample all PAs of particles for almost all expected magnetic field orientations as it points perpendicular to the spin axis of the spacecraft. REPT utilizes concurrent magnetic field and plasma wave observations (Baker et al., 2012) to study the dynamical evolution of both the energy and PAD of the highly relativistic population throughout the radiation belts (Li et al., 2015). The REPT instrument has 12 electron energy channels, each resolved at 17 PAs. For $L \leq 2$, the electron channels are contaminated due to the presence of background penetrating protons (Li et al., 2015), making electron flux measurements uncertain. Out of 12 available REPT energy channels, we excluded the two highest bins (15.2 and 20 MeV) that gives the integral electron flux, as these most often do not have statistically significant counts. Hence, we restrict our studies above $L = 3$ and electron energies between 1.8 and 7.7 MeV.

For analyzing the electron PAD, we employed the method approached by previous researches, for example, Vampola (1997) and Gannon et al. (2007), and we assume that the electron PAD fits well to the distribution of the type

$$J_{eq} = J_0 \sin^n(\alpha_{eq}) \tag{1}$$

here, J_{eq} is the differential electron flux at a given kinetic energy in the equatorial plane. J_0 is the flux at 90° PA and n is the power of the sine function, that is, any real number (i.e., can be negative). To avoid the contamination from the background fluxes, we excluded the values below 10^{-2}/cm^2·s·sr·MeV (Baker et al., 2012). The PA-distributed data are binned according to different L values, having bin size of 0.1L and averaged in time for each storm interval. Moreover, flux measurements made by Van Allen Probes A are limited to times when Probe A is near equatorial plane, that is MLat = ±10°. However, measurements spanning different storm phases may vary about ±3° from phase to phase of a given magnetic storm. Note that all measurements are still within MLat = ±10°. Within the L bin of 0.1 L and ±3° MLat, MLT varies by ±0.5 hr. The PA index n_1, n_2, and n_3 corresponds to the "prestorm," "at-storm," and "poststorm" intervals, respectively. The "prestorm" interval is considered as the interval before the time of storm sudden commencement; "at-storm" interval is the interval of storm main phase and "poststorm" interval is the interval after Dst minimum. To be precise, we adapted the definition of the terms "prestorm," "at-storm," and "poststorm" for CME- and CIR-driven storms, from Pandya et al. (2019), wherein they clearly defined the intervals for each category of the magnetic storms. The value of PA index "n" obtained from the fit to the sine function, indicates the type of electron PAD. For instance, a decrease in n value broadens and reduces the peak around 90° PA (i.e., leading to more isotropic distribution). We adapted the least square fitting method and quantified the goodness of the fit by normalized standard deviation as given in Ni et al. (2015). The standard deviation for ~92% of the observations fall <0.5. We selected a minimum of eight data points to fit electron PAD. The equatorial flux was calculated on the basis of the assumption that the first adiabatic invariant is conserved. The equatorial magnetic field was computed using OP77Q external field and IGRF internal field (Baker et al., 2012).

Figure 1 shows the typical equatorial PADs of electrons with energy of 2.1 MeV in the radiation belts that includes mainly, pancake PAD, butterfly PAD, and flattop PAD. PADs shown in Figure 1 are measured by the

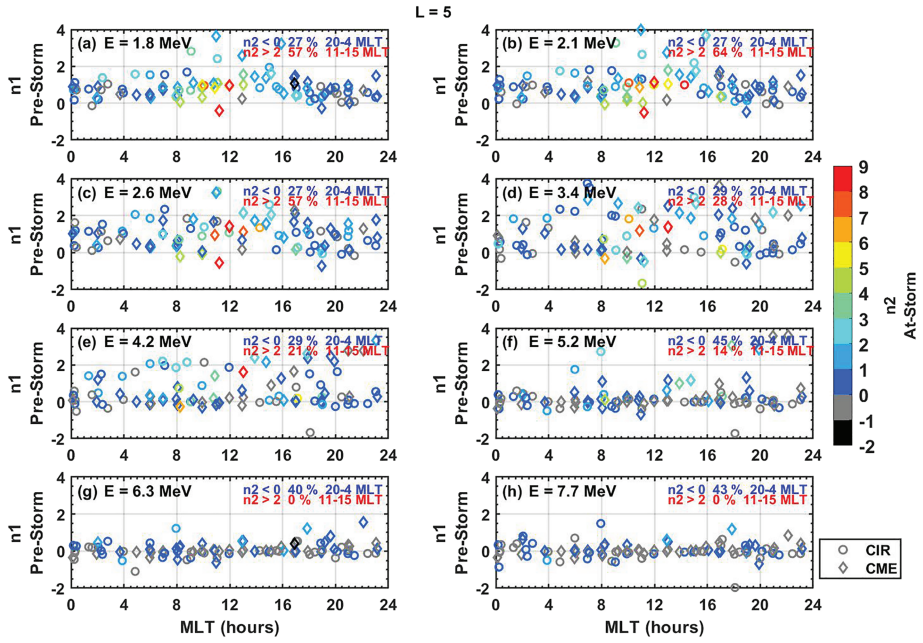

Figure 2. (a–h) Electron distribution fitted with power n_1 (prestorm) versus MLT is shown. The color scale represents the steepness of the distribution n_2 during "at-storm" interval. Each panel corresponds to the fitted powers at different energies for $L = 5$. Circle and diamond symbol represents the CIR storms and CME driven storms.

REPT instrument on Van Allen Probes at a given L value, MLT, and energy channel during different phase of the magnetic storm. Each top and bottom pair of panels refer to the electron flux measurements for four different MLT sectors: 00, 06, 12, and 18 at $L = 5$ (a–d) and $L = 3$ (e–h). Prestorm, at-storm, and poststorm intervals are indicated by black, red, and blue colors, respectively. Measured fluxes are indicated by open circles and the fit by the solid line. Since the electron fluxes are averaged over the magnetic storm phase interval, the gray colored lines show the statistical error bars indicating the range of variation within a given storm. For each phase of the storm, we fit $J_0 sin^n(\alpha_{eq})$ function and obtain values of n_1, n_2, and n_3 for each prestorm, at-storm, and poststorm intervals at nearly same magnetic latitude (MLat) of the spacecraft. At $L = 5$ and $E = 2.1$ MeV, a variety of electron PADs are observed for different MLT sectors (panels a–d). Magnetic storm shown in panel (a) exhibits nearly butterfly-like PAD during the prestorm interval ($n_1 \sim -0.1$) that evolves into more butterfly like during the storm main phase ($n_2 \sim -0.9$) in ~00 MLT. During the poststorm interval, the distribution turns to almost pancake like with n_3 ~1.2. At ~06 MLT (panel b), the distribution turns slightly pancake like during the at-storm interval, while the feature is more pronounced (n_2 ~5.92) very well for the events falling at ~12 MLT (panel c). At ~18 MLT (panel d) the electron PADs appears to be nearly flattop like. Figures 1e–1h summarizes the equatorial PADs measured at L=3, showing that the flux peaks at 90° during all the three phases, indicating a stable, trapped distribution ($n > 0$) across all the MLT sectors at $L = 3$. Panels (e)–(h) shows no major evolution of electron PADs during a magnetic storm.

Based on the above criteria, we further confine our analysis to $L \geq 3$ from the REPT data set for 55 geomagnetic storms that occurred during the period from October 2012 to May 2017. The corresponding L value, MLT, energy channels, and PA-distributed electron flux is recorded to study the global occurrence of outer radiation belt.

3. Observation and Analysis

3.1. MLT Dependence of Electron PADs at Each Phase of the Magnetic Storm

To illuminate the signature of various PADs, we establish a robust data set of REPT observations during each phase of the magnetic storm. This helps to analyze the evolution of electron PADs and corresponding power (n) of the sine function fitting. We perform a least square fit of equation (1) to the equatorial electron differential flux as a function of PA at each interval to calculate the n value for each considered REPT energy channel. This characterizes the electron PAD at each L value, MLT, and energy, in addition to each phase

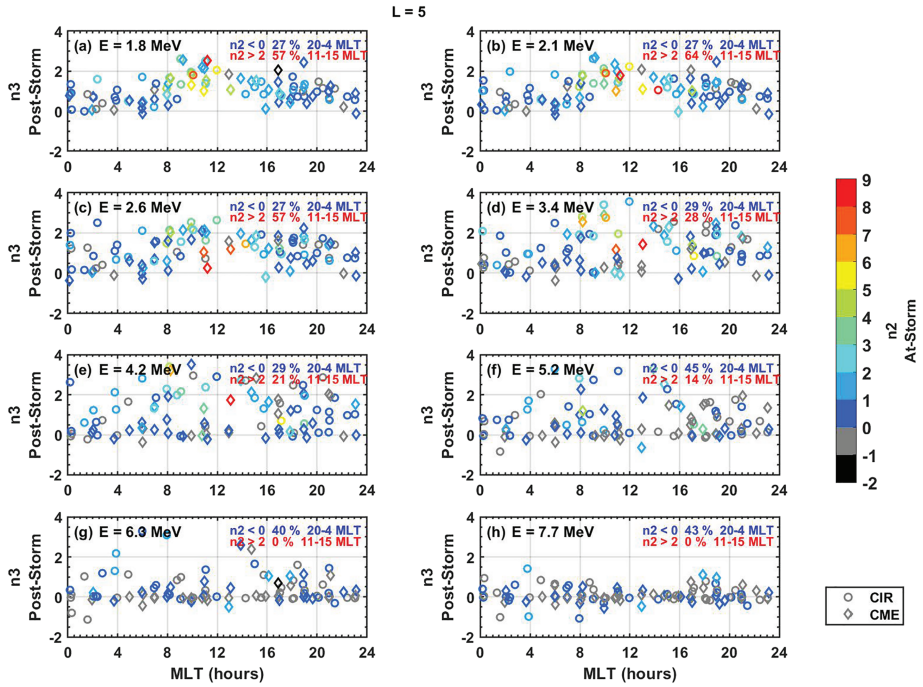

Figure 3. (a–h) Electron distribution fitted with power n_3 (poststorm) versus MLT is shown. The color scale represents the steepness of the distribution n_2 during "at-storm" interval. Each panel corresponds to the fitted powers at different energies for $L = 5$.

of the magnetic storm. We carried out the same analysis for each L value (i.e., $L = 3$, 4, and 5) however to illustrate, we present only the PAD evolution at the radiation belt boundaries (i.e., $L = 5$ and $L = 3$).

Figure 2 shows n_1 and n_2 as a function of MLT for energies ranging from 1.8 to 7.7 MeV at $L = 5$. Open circles and diamonds represent the n value for the CIR- and CME-driven magnetic storms. It is evident that n_1, n_2, and n_3 do not show any clear tendency of its MLT dependence beyond 7 MeV; hence, we restricted our studies to the energy range of 1.8–7.7 MeV. A clear MLT dependence is observed at lower energy channels <3.4 MeV (panels a–c). During midnight sector n_1 values are close to 0 ($-1 \leq n_1 \leq 2$), showing nearly flattop PADs, while n_1 varies from $-1 \leq n_1 \leq 4$ during noon sectors. On the other hand, during at-storm interval a peculiar type of distribution pattern appears. For majority of the magnetic storms, the storm time electron PAD (i.e., n_1 and n_2) varies considerably across all the MLT sectors for $E < 3.4$ MeV. For $E \leq 3.4$ MeV, relativistic electron PAD varies over a wide range of n_2 values that show a clear color distinction from red to blue in the noon to midnight sectors. Storm time electron PAD fits yield $n_2 \leq 1$ in the midnight sector, while n_2 varies upto 9 during the noon sectors. This indicates that the at-storm electron PAD is either flattop or butterfly like in the nightside, while it is pancake like in the noon sector. For energies ≤3.4 MeV, the magnitude of change of n_1 and n_2 during the noontime is observed to be about 3 or more, while it is about one or two in the nightside. It is worth to estimate the difference between two PA indices, as it directly reflected the change in electron PADs. The statistical outcome of at-storm electron PADs (n_2) at different energies is given in each figure panel in the group of two time intervals, 20–04 and 11–15 MLT. As can be seen from Figure 2, at $L = 5$ and $E < 3.4$ MeV, ~30% n_2 values are observed with $n_2 < 0$ in 20–4 MLT sectors (blue). Contrarily, during the noon sector, that is, from 11–15 MLT, more than 60% of cases show $n_2 > 2$ (red). Interestingly, this tendency diminishes for higher-energy channels (≥3.4 MeV).

Figure 3 shows the results of our analysis of evolution of electrons PADs during the poststorm interval. The panel representation of Figure 3 is same as Figure 2 except for n_2 and n_3 values of the fit as a function of MLT. We find that for $E \leq 3.4$ MeV, the poststorm electron PADs tend to the flattop type during the storm recovery phase. The distribution becomes trapped-like across all the MLT sectors, with n_3 values ranging from 0 to 4 for $E \leq 2.1$ MeV, while it ranges from −2 to 4 for $E \geq 2.6$ MeV. The difference in the index of the power n_3 and n_2 is about 3 or more in the noontime, while it is about 2 or less in the nightside. The MLT dependence of electron PADs is regardless of the storm driver, while the at-storm statistics remain same as before

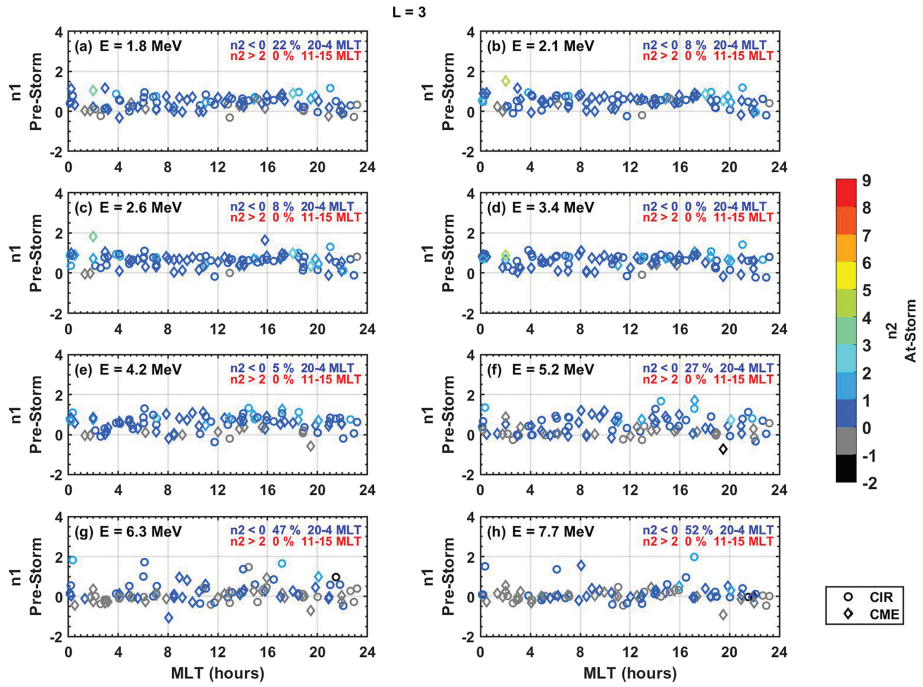

Figure 4. The panel representations are same as Figure 2, except for $L = 3$.

(i.e., as shown in Figure 2). We find from Figure 2 and 3 that there is not much difference in the electron PADs during CME- and CIR-driven storms.

The evolution of storm time electron PADs at L = 3, that is, the inner edge of the outer radiation belt, is shown in Figure 4. The panel representations of Figure 4 are same as Figure 2, except for $L = 3$. From Figure 4 we find that n_1 ranges between −1 and 2 for all the energy channels but a majority of the electron PADs remain stably trapped ($n_1 > 0$) during the prestorm interval. During at-storm interval, the PA index

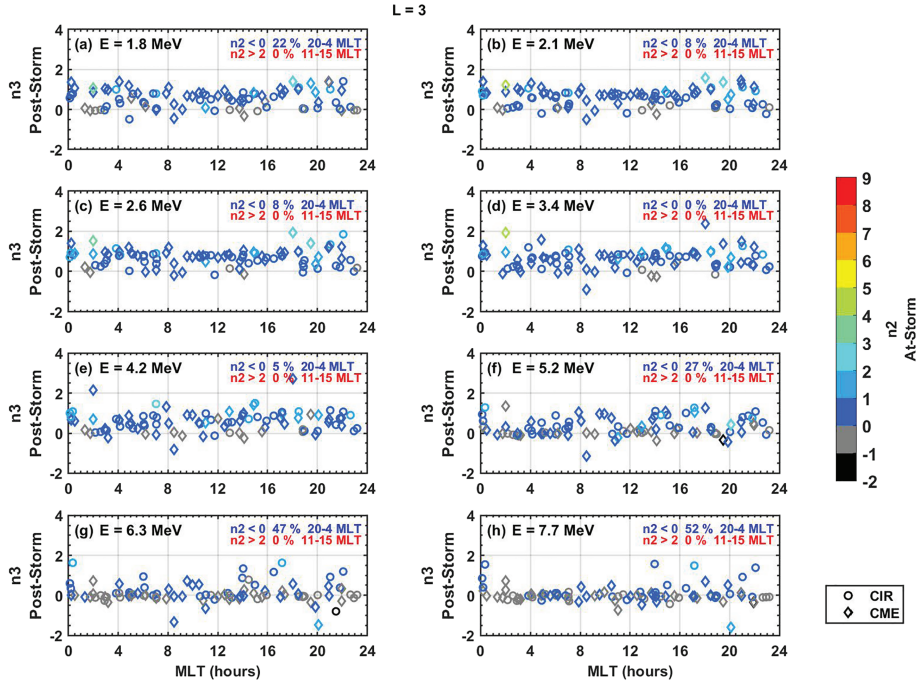

Figure 5. The panel representations are same as Figure 3, except for $L = 3$.

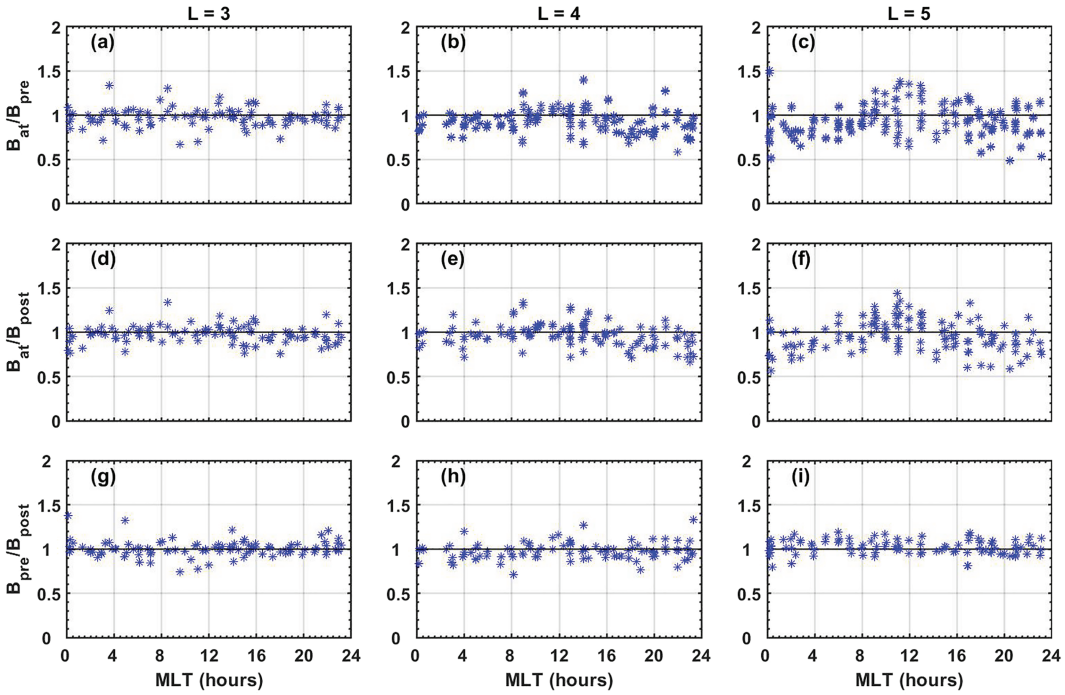

Figure 6. MLT distribution of the magnetic field ratios for $L = 3$, 4, and 5 during (a–c) at-storm to prestorm B_{at}/B_{pre} and (d–f) poststorm to at-storm B_{post}/B_{at}.

n_2 remains at lower values (n_2 ~0), indicating only a slight distinction of electron PAD from the prestorm interval. Below 4.2 MeV (panels a–d), the flattop, trapped distribution persists across all MLT sectors, while a few butterfly PAD appear for >4.2 MeV energies (e–h), irrespective of the storm driver. Statistically, we do not find any significant MLT dependence of the electron PADs on MLTs. Additionally, Figure 4 shows that n_1 and n_2 values vary very slightly (<2) across all the MLT sectors and entire band of energies. There is not much difference in the change of distribution from prestorm to at-storm interval.

To study the poststorm signatures of electron PADs at $L = 3$, we show Figure 5, which is same as Figure 3 except for $L = 3$. From Figure 5, it is evident that there is no well defined contrast in the electron PADs between at-storm and poststorm intervals. The n_2 and n_3 values remain close to 0, and their difference is very low (<2). For energies <4.2 MeV (panels a–d), the n_3 values are larger than 0, that is, flattop like across all the MLT sectors, which turns butterfly like at higher energies (panels e–h). In short, there is no MLT dependence of radiation belt electron PADs, at $L = 3$, during main phase or recovery phase of the magnetic storm and is highly independent of the magnetic storm driver. Though not shown here, the electron PADs at $L = 4$ appears to be in a transition state between $L = 3$ and $L = 5$. It is noteworthy to understand that the electron PADs with 90° minima are present across all the MLT sectors for the higher energy channels (>4.2 MeV). This can be attributed to the fact that electron flux that is very low and too close to the background, to get any clear signatures of PAD. To understand the underlying physical processes, we investigate further the related magnetic field changes, which may provide the plausible mechanism for electron flux response.

3.2. Magnetic Field Reconfiguration During a Magnetic Storm

Figure 6 represents the total magnetic field (B) variations during the different phases of the magnetic storms. To study the relative changes from one storm phase to other, we show the ratio of averaged total magnetic field during each phase. Panels (a)–(c) represent the magnetic field variations across different MLT sectors during the prestorm and at-storm intervals for $L = 3$, 4, and 5. From panel (a), it can be seen that the magnetic field does not show any significant changes or any particular MLT dependence. The observations at $L = 4$ (panel b) shows a slight enhancement in the noon sector, which enhances further and becomes more pronounced at $L = 5$ (panel c). Furthermore, the total magnetic field during at-storm interval decreases on the nightside. Hence, there is a strong day-night asymmetry in the magnetic field configuration with L values. Panel (d) represents the poststorm magnetic field variations at $L = 3$. It can be inferred that there are no substantial magnetic storm effects on the Earth's magnetic field at $L = 3$. At $L = 4$, slight noontime

depression in the Earth's magnetic field is observed during the storm recovery phase. However, the magnetic field reduction in the noon-time and enhancement in the dayside becomes more evident for $L = 5$. The magnetic field tries to restore its original configuration during the poststorm interval.

Distorted nondipolar magnetospheric magnetic field alone could be responsible for the changes in the trapped population in the Earth's inner magnetosphere (Sibeck et al., 1987). The isotropic PADs appear as the electron flux does not vary so greatly with PA. These PADs are typically attributed to the interaction of drifting particles with a region of strong turbulence or sharp magnetic field gradients. The magnetic field in the lower L shells is nearly dipolar and for this configuration, all particles follow the circular drift paths leaving inner magnetospheric flux nearly unaltered during any phase of the magnetic storm. However, these magnetic field changes cannot fully explain the energy dependent PAD changes.

4. Discussion

4.1. MLT Dependence of Electron PADs at Higher *L* Region

The day-night asymmetry of the electron PAD is clearly seen at $L = 5$. This is due to the fact that the Earth's magnetic field becomes more dynamic under the influence of solar wind conditions and the intensification of the ring current. At $L = 5$, the electron flux at 90 degree PA decreases on the nightside, while it increases on the dayside as shown in Figures 2 and 3. As the magnetic storm progresses from prestorm to at-storm interval, the electron PAD changes from trapped pancake like to butterfly like on the nightside and strongly pancake like on the dayside. After the magnetic storm has passed, the electron PADs tend to recover back to the prestorm configuration. This tendency is clearly found at particular energy range between 1.8 and 2.6 MeV. The day-night asymmetry of the PAD may be explained in terms of adiabatic processes. One such process that has long been recognized is drift-shell splitting, arising from the day-night asymmetry of the Earth's magnetic field strength (Stone, 1963; Roederer, 1967). The dayside magnetosphere is compressed by the magnetopause current, whereas the nightside magnetic field is stretched (weakened) by the tail current and the ring current. Equatorially mirroring particles drift along the constant magnetic field. The radial distance of the drift trajectory is longer on the dayside than on the nightside. Contrarily, the bounce-averaged drift trajectories of more field-aligned particles tend to encircle the Earth at almost the same radial distance. This may cause the butterfly-like distribution (e.g., West et al., 1973). Indeed, the geomagnetic field is observed to increase on the dayside. Another process is adiabatic acceleration/deceleration of particles. When the ring current develops, the equatorial magnetic field decreases in the inner magnetosphere, resulting in adiabatic deceleration. This adiabatic deceleration decreases the near field-perpendicular particle fluxes (McIlwain, 1966). At the same time, the magnetic field increases at off-equator, giving rise to adiabatic acceleration of the near-field-aligned particles (Ebihara et al., 2008). Both the adiabatic acceleration/deceleration cause the butterfly-like PAD. The pancake-like PADs found on the dayside may be explained by the flux depending on L. Let us consider particles located at some point on the dayside. The near-field-aligned particles come from the nightside at almost the same L, whereas the near-field-perpendicular particle come from the nightside closer to the near field-aligned one because of drift shell splitting. If the near-field-perpendicular flux at inner L is larger than the near field-parallel flux at outer L, the pancake-like PAD will appear on the dayside, while the opposite thing can occur on the nightside.

Our observations of the day-night PAD asymmetry of MeV electrons is consistent with the theoretical assumptions of drift shell splitting and radial diffusion as explained by Zhao et al. (2018). The changes in the geomagnetic field configuration potentially affects the radial flux gradient caused by magnetopause shadowing. However, for the complete understanding of the globally distributed PA-resolved electrons, future simulation, and modeling would be helpful to underline the underlying physical mechanism.

4.2. MLT Dependence of Electron PADs at Lower *L* Region

The major significant result from Figures 4 and 5 is the lower values of n_1, n_2, and n_3 of fitted PA-resolved electron flux at $L = 3$. The distribution remains almost unaltered during any phase of the magnetic storm and there is no particular dependence on MLTs. We note that during a magnetic storm, electron flux with $(0<n<1)$ PADs are present at all the times on the inner edge of the outer belt. The results are consistent with the existing theories of highly 90° peaked PAD inside lower radiation belt region (Lyons et al., 1972; Lyons & Williams, 1975a, 1975b). Our results are also highly consistent with the recent observations from MagEIS as reported by (Zhao et al., 2014). Investigating the effects on the Earth's magnetic field on electron PADs (as shown in Figure 6), we observed that there is no significant variation. The magnetic field remains nearly

undistorted and uniform across all the MLT sectors. Our statistical studies suggest that there may be other processes responsible for the observed PAD variability across L and energy.

5. Summary

A detailed study of the electron PADs in the outer radiation belt has been performed using the REPT measurements for the magnetic storms that occurred during the period from October 2012 to May 2017. Systematically, we complied a rich data set by fitting $J_0 sin^n(\alpha_{eq})$ function to the electron PADs that captures the dynamical evolution of PAD of the relativistic electron during each phase of the magnetic storm. The dependence of the PAD of relativistic electrons on temporal, spatial and energy were found to be significant. The major findings from this study are summarized as follows:

(1) At L~5, the PAD of the electrons varies according to the phase of the magnetic storm. PADs are broad and flat before the onset of the magnetic storm (n_1 ~0). During at-storm interval, it evolves differently in different MLT sectors and returns back to flattop type configuration during the poststorm.
(2) For E <3.4 MeV, the "at-storm" electron PADs change from pancake to butterfly type from noon to midnight sector at $L = 5$. For $E \leq$3.4 MeV, the electron PADs are highly 90° peaked (n_2>3) on the dayside, while flattop to butterfly like on the nightside. This could be attributed to the radial diffusion in conjunction with drift shell splitting. The changes can be explained, only in part, by the adiabatic processes.
(3) Conversely, the electron PADs at $L = 3$ are not significantly affected by the geomagnetic storms in the entire band of energies (1.8–7.7 MeV). The PADs are predominantly trapped-like (n_2 ~≥0) across all the MLT sectors and do not show any significant change from one phase of the magnetic storm to another.
(4) Storm time magnetic field does not vary so considerably at $L = 3$, while a characteristic day-night asymmetry is observed at $L = 5$. The solar wind compresses the dayside magnetic field and elongates it in the nightside. This enhances it during the dayside, while reducing on the night.
(5) The MLT dependence of electron PADs is irrespective of the magnetic storm driver.

Acknowledgments
The authors sincerely thank G. D. Reeves for helpful discussion and encouragement toward this work, during AP-RASC URSI-2019 meeting. The authors sincerely thank Van Allen Probes REPT data team for making REPT data publically available on http://www.rbsp-ect.lanl.gov/science/DataDirectories.php website.

References

Baker, D. N., Blake, J. B., Klebesadel, R. W., & Higbie, P. R. (1986). Highly relativistic electrons in the Earth's outer magnetosphere: 1. Lifetimes and temporal history 1979–1984. *Journal of Geophysical Research*, *91*(A4), 4265–4276. https://doi.org/10.1029/ja091ia04p04265

Baker, D. N., Kanekal, S. G., Hoxie, V. C., Batiste, S., Bolton, M., Li, X., et al. (2012). The Relativistic Electron-Proton Telescope (REPT) instrument on board the Radiation Belt Storm Probes (RBSP) spacecraft: Characterization of earth's radiation belt high-energy particle populations. In N. Fox & J. L. Burch (Eds.), *The Van Allen Probes Mission* (pp. 337–381). Boston, MA: Springer. https://doi.org/10.1007/978-1-4899-7433-4_11

Baker, D. N., Kanekal, S. G., Hoxie, V. C., Henderson, M. G., Li, X., Spence, H. E., et al. (2013). A long-lived relativistic electron storage ring embedded in Earth's outer Van Allen Belt. *Science*, *340*(6129), 186–190. https://doi.org/10.1126/science.1233518

Blake, J. B., Kolasinski, W. A., Fillius, R. W., & Mullen, E. (1992). Injection of electrons and protons with energies of tens of MeV into l< 3 on 24 March 1991. *Geophysical Research Letters*, *19*(8), 821–824. https://doi.org/10.1029/92GL00624

Carbary, J. F., Mitchell, D. G., Paranicas, C., Roelof, E. C., Krimigis, S. M., Krupp, N., et al. (2011). Pitch angle distributions of energetic electrons at saturn. *Journal of Geophysical Research*, *116*, A01216. https://doi.org/10.1029/2010JA015987

Chen, Y., Friedel, R. H. W., Henderson, M. G., Claudepierre, S. G., Morley, S. K., & Spence, H. E. (2014). Repad: An empirical model of pitch angle distributions for energetic electrons in the earth's outer radiation belt. *Journal of Geophysical Research: Space Physics*, *119*, 1693–1708. https://doi.org/10.1002/2013JA019431

Ebihara, Y., Fok, M.-C., Blake, J. B., & Fennell, J. F. (2008). Magnetic coupling of the ring current and the radiation belt. *Journal of Geophysical Research*, *113*, A07221. https://doi.org/10.1029/2008JA013267

Friedel, R. H. W., Reeves, G. D., & Obara, T. (2002). Relativistic electron dynamics in the inner magnetosphere—A review. *Journal of Atmospheric and Solar-Terrestrial Physics*, *64*(2), 265–282. https://doi.org/10.1016/s1364-6826(01)00088-8

Gannon, J. L., Li, X., & Heynderickx, D. (2007). Pitch angle distribution analysis of radiation belt electrons based on combined release and radiation effects satellite medium electrons a data. *Journal of Geophysical Research*, *112*, A05212. https://doi.org/10.1029/2005JA011565

Horne, R. B., Meredith, N. P., Thorne, R. M., Heynderickx, D., Iles, R. H. A., & Anderson, R. R. (2003). Evolution of energetic electron pitch angle distributions during storm time electron acceleration to megaelectronvolt energies. *Journal of Geophysical Research*, *108*(A1), 1016. https://doi.org/10.1029/2001JA009165

Kanekal, S. G. (2006). A review of recent observations of relativistic electron energization in the Earth's outer Van Allen radiation belt. In N. Gopalswamy & A. Bhattacharyya (Eds.), *Proceedings of the ILWS Workshop on Solar Influence on the Heliosphere and Earth's Environment* (pp. 274–279). Goa, India: Quest Publishers.

Li, W., Shprits, Y. Y., & Thorne, R. M. (2007). Dynamic evolution of energetic outer zone electrons due to wave-particle interactions during storms. *Journal of Geophysical Research*, *112*, A10220. https://doi.org/10.1029/2007JA012368

Li, X., Selesnick, R. S., Baker, D. N., Jaynes, A. N., Kanekal, S. G., Schiller, Q., et al. (2015). Upper limit on the inner radiation belt MeV electron intensity. *Journal of Geophysical Research: Space Physics*, *120*, 1215–1228. https://doi.org/10.1002/2014ja020777

Lyons, L. R., Thorne, R. M., & Kennel, C. F. (1972). Pitch-angle diffusion of radiation belt electrons within the plasmasphere. *Journal of Geophysical Research*, *77*(19), 3455–3474. https://doi.org/10.1029/ja077i019p03455

Lyons, L. R., & Williams, D. J. (1975a). The quiet time structure of energetic (35–560 keV) radiation belt electrons. *Journal of Geophysical Research*, *80*(7), 943–950. https://doi.org/10.1029/ja080i007p00943

Lyons, L. R., & Williams, D. J. (1975b). The storm and poststorm evolution of energetic (35–560 keV) radiation belt electron distributions. *Journal of Geophysical Research*, *80*(28), 3985–3994. https://doi.org/10.1029/ja080i028p03985

McIlwain, C. E. (1966). Ring current effects on trapped particles. *Journal of Geophysical Research*, *71*(15), 3623–3628. https://doi.org/10.1029/jz071i015p03623

Ni, B., Zou, Z., Gu, X., Zhou, C., Thorne, R. M., Bortnik, J., et al. (2015). Variability of the pitch angle distribution of radiation belt ultra-relativistic electrons during and following intense geomagnetic storms: Van Allen probes observations. *Journal of Geophysical Research: Space Physics*, *120*, 4863–4876. https://doi.org/10.1002/2015JA021065

Ni, B., Zou, Z., Li, X., Bortnik, J., Xie, L., & Gu, X. (2016). Occurrence characteristics of outer zone relativistic electron butterfly distribution: A survey of Van Aallen Probes rept measurements. *Geophysical Research Letters*, *43*, 5644–5652. https://doi.org/10.1002/2016GL069350

Pandya, M., Veenadhari, B., Ebihara, Y., Kanekal, S. G., & Baker, D. N. (2019). Variation of radiation belt electron flux during cme and cir driven geomagnetic storms: Van Allen Probes observations. *Journal of Geophysical Research: Space Physics*, *124*, 6524–6540. https://doi.org/10.1029/2019JA026771

Reeves, G. D., McAdams, K. L., Friedel, R. H. W., & O'Brien, T. P. (2003). Acceleration and loss of relativistic electrons during geomagnetic storms. *Geophysical Research Letters*, *30*(10), 1529. https://doi.org/10.1029/2002GL016513

Roederer, J. G. (1967). On the adiabatic motion of energetic particles in a model magnetosphere. *Journal of Geophysical Research*, *72*(3), 981–992. https://doi.org/10.1029/jz072i003p00981

Schulz, M., & Lanzerotti, L. J. (1974). *Particle diffusion in the radiation belts*. NY: Springer.

Selesnick, R., & Kanekal, S. (2009). Variability of the total radiation belt electron content. *Journal of Geophysical Research*, *114*, A02203. https://doi.org/10.1029/2008JA013432

Selesnick, R. S., & Blake, J. B. (2002). Relativistic electron drift shell splitting. *Journal of Geophysical Research*, *107*(A9), 1265. https://doi.org/10.1029/2001JA009179

Sibeck, D. G., McEntire, R. W., Lui, A. T. Y., Lopez, R. E., & Krimigis, S. M. (1987). Magnetic field drift shell splitting: Cause of unusual dayside particle pitch angle distributions during storms and substorms. *Journal of Geophysical Research*, *92*(A12), 13,485–13,497. https://doi.org/10.1029/ja092ia12p13485

Spence, H. E., Reeves, G. D., Baker, D. N., Blake, J. B., Bolton, M., Bourdarie, S., et al. (2013). Science goals and overview of the Radiation Belt Storm Probes (RBSP) energetic particle, composition, and thermal plasma (ECT) suite on NASA's Van Allen Probes mission. *Space Science Reviews*, *179*(1-4), 311–336. https://doi.org/10.1007/s11214-013-0007-5

Stone, E. C. (1963). The physical significance and application of l, b 0, and r 0 to geomagnetically trapped particles. *Journal of Geophysical Research*, *68*(14), 4157–4166.

Thorne, R. M., Horne, R. B., Glauert, S., Meredith, N. P., Shprits, Y. Y., Summers, D., & Anderson, R. R. (2005). The influence of wave-particle interactions on relativistic electron dynamics during storms. *Geophysical Monograph-American Geophysical Union*, *159*, 101. https://doi.org/10.1029/159gm07

Turner, D. L., Angelopoulos, V., Morley, S. K., Henderson, M. G., Reeves, G. D., Li, W., et al. (2014). On the cause and extent of outer radiation belt losses during the 30 September 2012 dropout event. *Journal of Geophysical Research: Space Physics*, *119*, 1530–1540. https://doi.org/10.1002/2013ja019446

Vampola, A. L. (1997). Outer zone energetic electron environment update, Conference on the High Energy Radiation Background in Space, Institute of Electrical and Electronic Engineers, Snowmass, Colorado.

West, H. I., Buck, R. M., & Walton, J. R. (1973). Electron pitch angle distributions throughout the magnetosphere as observed on ogo 5. *Journal of Geophysical Research*, *78*(7), 1064–1081. https://doi.org/10.1029/ja078i007p01064

Wrenn, G. L., Johnson, J. F. E., & Sojka, J. J. (1979). Stable pancake distributions of low energy electrons in the plasma trough. *Nature*, *279*(5713), 512–514. https://doi.org/10.1038/279512a0

Zhao, H., Friedel, R. H. W., Chen, Y., Reeves, G. D., Baker, D. N., Li, X., et al. (2018). An empirical model of radiation belt electron pitch angle distributions based on Van Allen Probes measurements. *Journal of Geophysical Research: Space Physics*, *123*, 3493–3511. https://doi.org/10.1029/2018JA025277

Zhao, H., Li, X., Blake, J. B., Fennell, J. F., Claudepierre, S. G., Baker, D. N., et al. (2014). Peculiar pitch angle distribution of relativistic electrons in the inner radiation belt and slot region. *Geophysical Research Letters*, *41*, 2250–2257. https://doi.org/10.1002/2014GL059725